Theoretical investigations of misfit dislocations in Pd/MgO(001) interfaces

2005 J. Phys.: Condens. Matter 17 6149

(http://iopscience.iop.org/0953-8984/17/39/004)

INSTITUTE OF PHYSICS PUBLISHING JOURNAL OF PHYSICS: CONDENSED MATTER

J. Phys.: Condens. Matter **17** (2005) 6149–6172 doi:10.1088/0953-8984/17/39/004

Theoretical investigations of misfit dislocations in Pd/MgO(001) interfaces

Y Long[1], **N X Chen**[1,2] **and H Y Wang**[1]

[1] Department of Physics, Tsinghua University, Beijing 100084, People's Republic of China
[2] Institute for Applied Physics, University of Science and Technology, 100083, People's Republic of China

E-mail: longyao@tsinghua.org.cn

Received 19 May 2005, in final form 1 August 2005
Published 16 September 2005
Online at stacks.iop.org/JPhysCM/17/6149

Abstract

This paper investigates the properties of dislocations in Pd/MgO(001) interfaces. By constructing ideal and virtual interface structures and applying the Chen–Mobius inversion method, we obtain interatomic potentials Φ_{Pd-Mg} and Φ_{Pd-O} directly from *ab initio* adhesive energies. Then, by applying the above potentials, as well as using the atomistic relaxation and molecular dynamics methods, stable interface structures are obtained. For simplicity, we use a two-dimensional model to provide some clear physical pictures of the dislocations. There are two kinds of mechanisms of dislocation formation: one is insertion of an extra slice of Pd atoms; the other is increasing the number of Pd layers, to produce dislocations via the increasing misfit stress. Finally, three-dimensional models are investigated, with dislocations perpendicularly intersecting in the interface. The calculated interfacial distances are in agreement with experiments.

1. Introduction

Metal–ceramic interfaces are more and more important in catalytic converters, field effect transistors, anticorrosion coatings, and composite materials. In these fields, the interface plays a key role since it significantly influences the material properties in mechanics, optics, magnetism, electronics, etc.

MgO is an important substrate for growing metal films. On the one hand, the lattice structure of MgO is one of the simplest structures, the rock-salt structure. On the other hand, it is comparatively easy to obtain a clean MgO(100) surface with a small density of defects.

The Pd/MgO(001) interface is one of the most widely researched interfaces. Though the lattice parameter mismatch is relatively large (−7.8%), the interface is not complex. The fabrication of the Pd film on the MgO(001) surface is in cube on cube epitaxy; this process includes nucleation, growth, and coalescence of islands [1, 2]. A semi-coherent interface will

form ultimately, with a misfit dislocation network parallel to [110] and [1$\bar{1}$0] directions [3, 4]. Here the so-called semi-coherent interface means that the dislocation lines (DLs) distribute along the interface regularly. Therefore, Pd/MgO as a sample is widely used in studying interface structure, thin film growth, dislocation networks, etc, which is concerned in many technologies such as grazing incidence x-ray scattering (GIXS) [1, 2, 5, 6], transmission electron microscopy (TEM) [3, 4, 7, 8], atomic force microscopy (AFM) [9], etc.

Because of its simplicity, the Pd/MgO interface is also investigated by a variety of theoretical methods. Most of them were limited to *ab initio* types, for systems consisting of small amounts of atoms. In this work, the aims were focused on the deposited sites, interfacial distance, adhesive energy, electronic structure, etc [10–14]. The others were based on molecular dynamics (MD) or atomistic relaxation methods, which were used to study the structure and mechanical properties of the interface [15, 16]. However, the latter seemed to have difficulty in obtaining a credible potential across the interface. Furthermore, the study of the problem of dislocations in the interface, which occurs inevitably, has seldom been seen.

In this work, we mainly focus on two points related to Pd/MgO(001) interfaces: obtaining efficient interfacial pair potentials and studying the formation and distribution of the dislocations by the pair potentials. First, in section 2, the interatomic pair potentials across the interface are neatly derived with the Chen–Mobius inversion procedure from *ab initio* adhesive energy curves. A key step is solving the inverse problem by using a number-theoretic technique; it is otherwise difficult to work out. Then, in section 3, a series of properties related to dislocations in the interface are investigated using two-dimensional (2D) models, which include the dislocation structure, dislocation density, the possible Pd film thickness not violating an ideal interface and bond distribution, etc. Next, in section 4, we further study three-dimensional (3D) interface models of the adhesive energy and interface distance. Finally, in section 5, we give our conclusions and a discussion.

2. Obtaining the pair potentials across the interface

2.1. The formalism

In order to achieve interatomic pair potentials across Pd/MgO(001) interfaces, the Chen–Mobius inversion method is used in this paper. The method was proposed by Chen in 1990s [17, 18], on the basis of some techniques in number theory. Unlike the usual empirical approaches based on experimental data, this method helps us to obtain parameter-free pair potentials inverted from *ab initio* energy curves. The method has been successfully applied to various bulk materials, such as ionic crystals [19], rare earth compounds [20], and semiconductors [21]. Recently, we successfully applied this method to obtain pair potentials across Ag/MgO(001) interfaces [22]. The mathematical basis of the inversion technique applied to interfaces is the additive semigroup, rather than the multiplicative semigroup applied for bulk materials.

This method is built on the assumption that the adhesive energy of an interface can be expressed as the summation over all pair interactions between atoms across the interface. This is obviously a rough approximation because of the complexity of chemical bonds in a real metal–ceramic interface. However, we show that such a pair potential approach gives a reasonable description of the complex interfacial structures to some extent. This is not really a surprise to us because, in fact, the pair potential approach has been used widely to study complex material phenomena including those at interfaces [15, 16].

To reveal our method, we now describe in detail the process used for deriving the interaction potentials of Pd–Mg and Pd–O pairs, denoted as $\Phi_{\mathrm{Pd-Mg}}$ and $\Phi_{\mathrm{Pd-O}}$, across the interface. Since

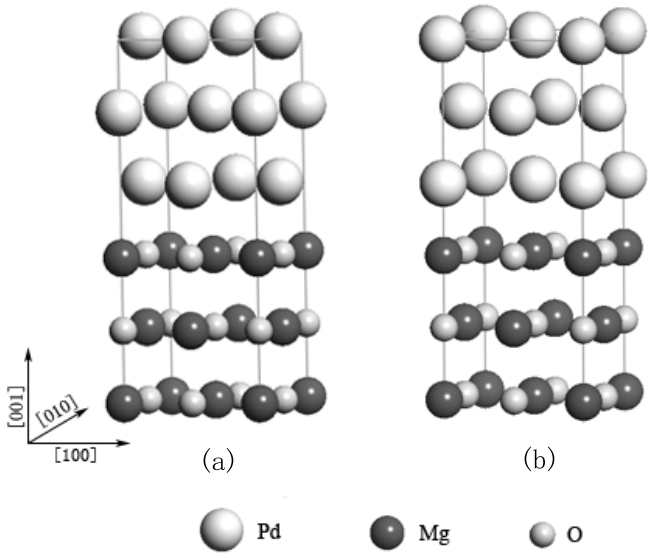

Figure 1. Pd/MgO(001) interface structures. (a) Pd upon O; unrelaxed ideal structure. (b) Pd upon Mg; virtual structure.

there are two functions to be obtained, we need two energy curves to invert the pair potentials. Therefore we should have two interface lattice structures. They are depicted in figure 1. The structure of figure 1(a) comes from experiments, in which Pd atoms are on top of O atoms. However, here the lattice constant of the Pd film is forced to be the same as that of the substrate MgO, denoted as a, so as to form a commensurate interface. Hence, it is called an ideal structure. Hereafter, when we say the ideal interface structure, we always mean that of figure 1(a). The structure in figure 1(b) is a virtual one, where Pd atoms are on top of Mg atoms.

The distance between the first-monolayer (ML) Pd atoms and the first-ML MgO atoms at the interface is denoted as x. The total energies of the two structures, figures 1(a) and (b), are denoted as $E_{\mathrm{O}}(x)$ and $E_{\mathrm{Mg}}(x)$ respectively. They can be expressed as

$$\begin{aligned}
E_{\mathrm{O}}(x) = \sum_{l,l'=0}^{\infty} \sum_{m,n=-\infty}^{\infty} \Big\{ & \Phi_{\mathrm{Pd-O}}\big(\sqrt{(x+la+l'a)^2+(ma)^2+(na)^2}\big) \\
& + \Phi_{\mathrm{Pd-O}}\big(\sqrt{(x+la+l'a)^2+((m+1/2)a)^2+((n+1/2)a)^2}\big) \\
& + \Phi_{\mathrm{Pd-O}}\big(\sqrt{(x+la+(l'+1/2)a)^2+(ma)^2+((n+1/2)a)^2}\big) \\
& + \Phi_{\mathrm{Pd-O}}\big(\sqrt{(x+la+(l'+1/2)a)^2+((m+1/2)a)^2+(na)^2}\big) \\
& + \Phi_{\mathrm{Pd-O}}\big(\sqrt{(x+(l+1/2)a+l'a)^2+(ma)^2+((n+1/2)a)^2}\big) \\
& + \Phi_{\mathrm{Pd-O}}\big(\sqrt{(x+(l+1/2)a+l'a)^2+((m+1/2)a)^2+(na)^2}\big) \\
& + \Phi_{\mathrm{Pd-O}}\big(\sqrt{(x+(l+1/2)a+(l'+1/2)a)^2+(ma)^2+(na)^2}\big) \\
& + \Phi_{\mathrm{Pd-O}}\big(\sqrt{(x+(l+1/2)a+(l'+1/2)a)^2+((m+1/2)a)^2+((n+1/2)a)^2}\big) \\
& + \Phi_{\mathrm{Pd-Mg}}\big(\sqrt{(x+la+l'a)^2+(ma)^2+((n+1/2)a)^2}\big) \\
& + \Phi_{\mathrm{Pd-Mg}}\big(\sqrt{(x+la+l'a)^2+((m+1/2)a)^2+(na)^2}\big) \\
& + \Phi_{\mathrm{Pd-Mg}}\big(\sqrt{(x+la+(l'+1/2)a)^2+(ma)^2+(na)^2}\big)
\end{aligned}$$

$$+\Phi_{\mathrm{Pd-Mg}}\left(\sqrt{(x+la+(l'+1/2)a)^2+((m+1/2)a)^2+((n+1/2)a)^2}\right)$$
$$+\Phi_{\mathrm{Pd-Mg}}\left(\sqrt{(x+(l+1/2)a+l'a)^2+(ma)^2+(na)^2}\right)$$
$$+\Phi_{\mathrm{Pd-Mg}}\left(\sqrt{(x+(l+1/2)a+l'a)^2+((m+1/2)a)^2+((n+1/2)a)^2}\right)$$
$$+\Phi_{\mathrm{Pd-Mg}}\left(\sqrt{(x+(l+1/2)a+(l'+1/2)a)^2+(ma)^2+((n+1/2)a)^2}\right)$$
$$+\Phi_{\mathrm{Pd-Mg}}\left(\sqrt{(x+(l+1/2)a+(l'+1/2)a)^2+((m+1/2)a)^2+(na)^2}\right)\Bigg\}, \quad (1)$$

$$E_{\mathrm{Mg}}(x)=\sum_{l,l'=0}^{\infty}\sum_{m,n=-\infty}^{\infty}\Bigg\{\Phi_{\mathrm{Pd-Mg}}\left(\sqrt{(x+la+l'a)^2+(ma)^2+(na)^2}\right)$$
$$+\Phi_{\mathrm{Pd-Mg}}\left(\sqrt{(x+la+l'a)^2+((m+1/2)a)^2+((n+1/2)a)^2}\right)$$
$$+\Phi_{\mathrm{Pd-Mg}}\left(\sqrt{(x+la+(l'+1/2)a)^2+(ma)^2+((n+1/2)a)^2}\right)$$
$$+\Phi_{\mathrm{Pd-Mg}}\left(\sqrt{(x+la+(l'+1/2)a)^2+((m+1/2)a)^2+(na)^2}\right)$$
$$+\Phi_{\mathrm{Pd-Mg}}\left(\sqrt{(x+(l+1/2)a+l'a)^2+(ma)^2+((n+1/2)a)^2}\right)$$
$$+\Phi_{\mathrm{Pd-Mg}}\left(\sqrt{(x+(l+1/2)a+l'a)^2+((m+1/2)a)^2+(na)^2}\right)$$
$$+\Phi_{\mathrm{Pd-Mg}}\left(\sqrt{(x+(l+1/2)a+(l'+1/2)a)^2+(ma)^2+(na)^2}\right)$$
$$+\Phi_{\mathrm{Pd-Mg}}\left(\sqrt{(x+(l+1/2)a+(l'+1/2)a)^2+((m+1/2)a)^2+((n+1/2)a)^2}\right)$$
$$+\Phi_{\mathrm{Pd-O}}\left(\sqrt{(x+la+l'a)^2+(ma)^2+((n+1/2)a)^2}\right)$$
$$+\Phi_{\mathrm{Pd-O}}\left(\sqrt{(x+la+l'a)^2+((m+1/2)a)^2+(na)^2}\right)$$
$$+\Phi_{\mathrm{Pd-O}}\left(\sqrt{(x+la+(l'+1/2)a)^2+(ma)^2+(na)^2}\right)$$
$$+\Phi_{\mathrm{Pd-O}}\left(\sqrt{(x+la+(l'+1/2)a)^2+((m+1/2)a)^2+((n+1/2)a)^2}\right)$$
$$+\Phi_{\mathrm{Pd-O}}\left(\sqrt{(x+(l+1/2)a+l'a)^2+(ma)^2+(na)^2}\right)$$
$$+\Phi_{\mathrm{Pd-O}}\left(\sqrt{(x+(l+1/2)a+l'a)^2+((m+1/2)a)^2+((n+1/2)a)^2}\right)$$
$$+\Phi_{\mathrm{Pd-O}}\left(\sqrt{(x+(l+1/2)a+(l'+1/2)a)^2+(ma)^2+((n+1/2)a)^2}\right)$$
$$+\Phi_{\mathrm{Pd-O}}\left(\sqrt{(x+(l+1/2)a+(l'+1/2)a)^2+((m+1/2)a)^2+(na)^2}\right)\Bigg\}, \quad (2)$$

where the variables in the right-hand side indicate the distance between Pd and O or between Pd and Mg. For example, in $\sqrt{(x+la+l'a)^2+(ma)^2+(na)^2}$, $(x+la+l'a)$ and $\sqrt{(ma)^2+(na)^2}$ are the components perpendicular to and parallel to the interface plane, respectively.

Deriving interfacial potentials $\Phi_{\mathrm{Pd-Mg}}(r)$ and $\Phi_{\mathrm{Pd-O}}(r)$ from energy curves $E_{\mathrm{Mg}}(x)$ and $E_{\mathrm{O}}(x)$ is not an easy job because equations (1) and (2) are complex equations with cross-coupling terms. A mathematical technique must be adopted in order to simplify the equations.

By defining

$$E_{\pm}(x)=E_{\mathrm{Mg}}(x)\pm E_{\mathrm{O}}(x) \quad (3)$$

and

$$\Phi_{\pm}(r)=\Phi_{\mathrm{Pd-Mg}}(r)\pm\Phi_{\mathrm{Pd-O}}(r), \quad (4)$$

we have

$$E_{\pm}(x)=\sum_{l,l'=0}^{\infty}\sum_{m,n=-\infty}^{\infty}\Bigg\{\Phi_{\pm}\left(\sqrt{(x+la+l'a)^2+(ma)^2+(na)^2}\right)$$
$$+\Phi_{\pm}\left(\sqrt{(x+la+l'a)^2+((m+1/2)a)^2+((n+1/2)a)^2}\right)$$

$$
\begin{aligned}
&+ \Phi_{\pm}(\sqrt{(x + la + (l' + 1/2)a)^2 + (ma)^2 + ((n + 1/2)a)^2}) \\
&+ \Phi_{\pm}(\sqrt{(x + la + (l' + 1/2)a)^2 + ((m + 1/2)a)^2 + (na)^2}) \\
&+ \Phi_{\pm}(\sqrt{(x + (l + 1/2)a + l'a)^2 + (ma)^2 + ((n + 1/2)a)^2}) \\
&+ \Phi_{\pm}(\sqrt{(x + (l + 1/2)a + l'a)^2 + ((m + 1/2)a)^2 + (na)^2}) \\
&+ \Phi_{\pm}(\sqrt{(x + (l + 1/2)a + (l' + 1/2)a)^2 + (ma)^2 + (na)^2}) \\
&+ \Phi_{\pm}(\sqrt{(x + (l + 1/2)a + (l' + 1/2)a)^2 + ((m + 1/2)a)^2 + ((n + 1/2)a)^2}) \\
&\pm \Phi_{\pm}(\sqrt{(x + la + l'a)^2 + (ma)^2 + ((n + 1/2)a)^2}) \\
&\pm \Phi_{\pm}(\sqrt{(x + la + l'a)^2 + ((m + 1/2)a)^2 + (na)^2}) \\
&\pm \Phi_{\pm}(\sqrt{(x + la + (l' + 1/2)a)^2 + (ma)^2 + (na)^2}) \\
&\pm \Phi_{\pm}(\sqrt{(x + la + (l' + 1/2)a)^2 + ((m + 1/2)a)^2 + ((n + 1/2)a)^2}) \\
&\pm \Phi_{\pm}(\sqrt{(x + (l + 1/2)a + l'a)^2 + (ma)^2 + (na)^2}) \\
&\pm \Phi_{\pm}(\sqrt{(x + (l + 1/2)a + l'a)^2 + ((m + 1/2)a)^2 + ((n + 1/2)a)^2}) \\
&\pm \Phi_{\pm}(\sqrt{(x + (l + 1/2)a + (l' + 1/2)a)^2 + (ma)^2 + ((n + 1/2)a)^2}) \\
&\pm \Phi_{\pm}(\sqrt{(x + (l + 1/2)a + (l' + 1/2)a)^2 + ((m + 1/2)a)^2 + (na)^2}) \Big\}. \qquad (5)
\end{aligned}
$$

Equation (5) is in fact two independent equations equivalent to equations (1) and (2). Once we are able to extract $\Phi_{\pm}(r)$ from $E_{\pm}(x)$, the interfacial potentials can be obtained from

$$\Phi_{\mathrm{Pd-Mg}} = \frac{\Phi_+ + \Phi_-}{2} \qquad \text{and} \qquad \Phi_{\mathrm{Pd-O}} = \frac{\Phi_+ - \Phi_-}{2}. \qquad (6)$$

From equation (5), $E_{\pm}(x)$ can be rewritten using $\Phi_{\pm}(r)$ in a more compact way such that

$$E_{\pm}(x) = \sum_{i,j=0}^{\infty} \sum_{s,t=-\infty}^{\infty} (\pm 1)^{i+j+s+t} \Phi_{\pm}(\sqrt{(x + (i + j)a/2)^2 + (s^2 + t^2)(a/2)^2}). \qquad (7)$$

If we define a new function $H_{\pm}(x)$:

$$H_{\pm}(x) = \sum_{s,t=-\infty}^{\infty} (\pm 1)^{s+t} \Phi_{\pm}(\sqrt{x^2 + (s^2 + t^2)(a/2)^2}), \qquad (8)$$

$E_{\pm}(x)$ can then be expressed using $H_{\pm}(x)$ as

$$E_{\pm}(x) = \sum_{i,j=0}^{\infty} (\pm 1)^{i+j} H_{\pm}(x + (i + j)a/2). \qquad (9)$$

From equation (9), we have

$$E_{\pm}(x) \mp E_{\pm}(x + a/2) = \sum_{j=0}^{\infty} (\pm 1)^j H_{\pm}(x + ja/2) \qquad (10)$$

and

$$E_{\pm}(x + a/2) \mp E_{\pm}(x + a) = \sum_{j=0}^{\infty} (\pm 1)^j H_{\pm}(x + ja/2). \qquad (11)$$

Therefore, $H_{\pm}(x)$ can in turn be expressed using $E_{\pm}(x)$ in the following way:

$$
\begin{aligned}
H_{\pm}(x) &= (E_{\pm}(x) \mp E_{\pm}(x + a/2)) \mp (E_{\pm}(R + a/2) \mp E_{\pm}(x + a)) \\
&= E_{\pm}(x) \mp 2E_{\pm}(x + a/2) + E_{\pm}(x + a). \qquad (12)
\end{aligned}
$$

Next, we try to obtain the inverted formula from equation (8), i.e., to express $\Phi_{\pm}(x)$ using $H_{\pm}(x)$. Equation (8) is rewritten as

$$H_{\pm}(x) = \sum_{n=0}^{\infty} (\pm 1)^n h(n) \Phi_{\pm}(\sqrt{x^2 + n(a/2)^2}), \tag{13}$$

where $h(n)$ is the coefficient defined as

$$h(n) = \begin{cases} 1 & \text{if } n = 0, \\ 4 & \text{if } n = s^2 \text{ or } 2s^2 \qquad \text{with } s \neq 0, \\ 8 & \text{if } n = s^2 + t^2 \qquad \text{with } 0 \neq |s| \neq |t| \neq 0, \\ 0 & \text{if } n \neq s^2 + t^2. \end{cases} \tag{14}$$

Note that once the case of $s_1^2 + t_1^2 = n = s_2^2 + t_2^2$ with $(s_1, t_1) \neq (s_2, t_2)$ occurs, we have to consider all the possible combinations. For example, $s_1^2 + t_1^2 = n = s_2^2 + t_2^2$ with $s_1^2 = t_1^2$ and $0 \neq s_2^2 \neq t_2^2 \neq 0$; thus $h(n) = 4 + 8 = 12$. A concrete example is $(s_1, t_1) = (5, 5)$ and $(s_2, t_2) = (1, 7)$ with $n = 50$.

For a set of coefficients $h(n)$, there exist inversion coefficients $g(n)$ satisfying a recursive relation

$$\sum_{m=0}^{n} h(m) g(n - m) = \delta_{n,0}, \tag{15}$$

where $\delta_{n,0}$ is the Kronecker function satisfying

$$\delta_{n,0} = \begin{cases} 1 & n = 0, \\ 0 & n \geqslant 1. \end{cases} \tag{16}$$

By the use of equations (15) and (16), one easily proves from equation (8) that

$$\begin{aligned} &\sum_{k=0}^{\infty} (\pm 1)^k g(k) H_{\pm}(\sqrt{x^2 + k(a/2)^2}) \\ &\quad = \sum_{k=0}^{\infty} (\pm 1)^k g(k) \sum_{m=0}^{\infty} (\pm 1)^m h(m) \Phi_{\pm}(\sqrt{x^2 + k(a/2)^2 + m(a/2)^2}) \\ &\quad = \sum_{n=0}^{\infty} (\pm 1)^n \Big(\sum_{m=0}^{n} h(m) g(n - m)\Big) \Phi_{\pm}(\sqrt{x^2 + n(a/2)^2}) \\ &\quad = \sum_{n=0}^{\infty} (\pm 1)^n \delta_{n,0} \Phi_{\pm}(\sqrt{x^2 + n(a/2)^2}) = \Phi_{\pm}(x). \end{aligned} \tag{17}$$

Thus we obtain the inversion of equation (8):

$$\Phi_{\pm}(x) = \sum_{n=0}^{\infty} (\pm 1)^n g(n) H_{\pm}(\sqrt{x^2 + n(a/2)^2}). \tag{18}$$

Now we have two equations (18) and (12), which enable us to invert the pair potentials $\Phi_{\pm}(r)$ from the adhesive energies $E_{\pm}(x)$:

$$\begin{aligned} \Phi_{\pm}(x) = \sum_{n=0}^{\infty} (\pm 1)^n g(n) \big(&E_{\pm}(\sqrt{x^2 + n(a/2)^2}) \mp 2E_{\pm}(\sqrt{x^2 + n(a/2)^2} + a/2) \\ &+ E_{\pm}(\sqrt{x^2 + n(a/2)^2} + a)\big). \end{aligned} \tag{19}$$

Here it should be noted that although the argument is x, the interfacial distance, the pair potential $\Phi_{\pm}(r)$ is valid for any distance across the interface.

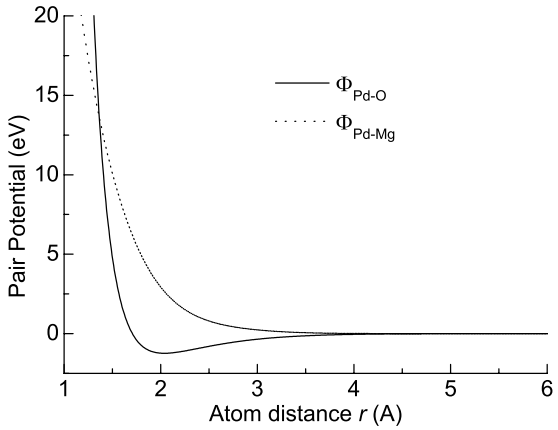

Figure 2. Pd–O and Pd–Mg interatomic pair potentials across the Pd/MgO(001) interface as functions of the atomic distance r.

It should pointed out that the above inversion procedure is suitable not only for the Pd/MgO(001) interface, but also for many other similar interface systems, such as Cu/MgO, V/MgO and Fe/MgO. For consistency with our early works [19–21], this method is called the Chen–Mobius inversion method.

We should emphasize here the discrepancy between inversions from the interface and from the bulk. The inversion coefficients $g(n)$ in the case of an interfacial potential are given by an additive recursive relation, equation (15), which corresponds to the Mobius inversion of the additive semigroup, while the inversion coefficients $g(n)$ in the case of the bulk material potential [19–21] were given by a multiplicative recursive relation,

$$\sum_{m|n} h(m)g(n/m) = \delta_{n1}, \tag{20}$$

which corresponds to the Mobius inversion of the multiplicative semigroup.

2.2. *The inverted pair potentials*

Now we are in a position to give the form of the pair potentials using equations (19) and (6). The total energies are obtained by *ab initio* calculation using CASTEP [23, 24] using an ultrasoft pseudopotential under the generalized gradient approximation (GGA). The plane-wave cut-off energy is 340 eV. The k-points are generated using the Monkhorst–Pack scheme, with the parameters (11 11 2) [25, 26]. In the reduced Brillouin zone, 21 k-points are taken.

The resulting Pd–Mg and Pd–O pair potential curves are plotted in figure 2 and they are fitted into the Rahman–Stillinger–Lemberg potential (RSL2) form:

$$\Phi_{\text{pair}}(r) = D_0 \mathrm{e}^{y(1-\frac{r}{R_0})} + \frac{a_1}{1+\mathrm{e}^{b_1(r-c_1)}} + \frac{a_2}{1+\mathrm{e}^{b_2(r-c_2)}} + \frac{a_3}{1+\mathrm{e}^{b_3(r-c_3)}}, \tag{21}$$

where $\Phi_{\text{pair}}(r)$ is $\Phi_{\text{Pd–Mg}}(r)$ or $\Phi_{\text{Pd–O}}(r)$. The related parameters are listed in table 1.

In this paper, we have to calculate the total energy of the interface structure using our inverted pair potentials. To do so, besides $\Phi_{\text{Pd–Mg}}(r)$ or $\Phi_{\text{Pd–O}}(r)$ which are for across the interface, the interatomic pair potentials in bulk Pd, $\Phi_{\text{Pd–Pd}}(r)$, and those in bulk MgO, $\Phi_{\text{Mg–Mg}}(r)$, $\Phi_{\text{O–O}}(r)$, and $\Phi_{\text{Mg–O}}(r)$, are also needed. These pair potentials have already been derived by the Chen–Mobius inversion method [27, 28]. $\Phi_{\text{Pd–Pd}}(r)$ has the form of a Morse

Table 1. Parameters of pair potentials across Pd/MgO(001).

Atom pair	Parameters		
Pd–Mg	$D_0 = 594.7397$ kcal mol^{-1}	$R_0 = 1.0000$ Å	$y = 2.8209$
	$a_1 = 163.0979$ kcal mol^{-1}	$b_1 = 3.5808$ Å^{-1}	$c_1 = 1.5548$ Å
	$a_2 = -133.8143$ kcal mol^{-1}	$b_2 = 2.7741$ Å^{-1}	$c_2 = 0.6426$ Å
	$a_3 = 2.9821$ kcal mol^{-1}	$b_3 = 4.2962$ Å^{-1}	$c_3 = 3.0629$ Å
Pd–O	$D_0 = 5704.9818$ kcal mol^{-1}	$R_0 = 1.0000$ Å	$y = 2.5470$
	$a_1 = -4705.3553$ kcal mol^{-1}	$b_1 = 3.3548$ Å^{-1}	$c_1 = 1.1077$ Å
	$a_2 = -862.3565$ kcal mol^{-1}	$b_2 = 2.2658$ Å^{-1}	$c_2 = 1.5894$ Å
	$a_3 = 0.3272$ kcal mol^{-1}	$b_3 = 2.8849$ Å^{-1}	$c_3 = 4.9511$ Å

Table 2. Parameters of short-range parts and the effective charge of the Coulomb part in the pair potentials for MgO bulk material.

		Short-range part			Coulomb part
Atom pair	Function form	D_0 (kcal mol^{-1})	R_0 (Å)	y	Q_{eff}
Mg–Mg	Morse	19.7866	2.42	9.96	
O–O	Morse	19.9871	2.36	9.45	$2.0e$
Mg–O	'exp-repulsive'	25.21	2.45	5.98	

potential, which is given as

$$\Phi_{\text{Pd–Pd}}(r) = D_0[\mathrm{e}^{-y(\frac{r}{R_0}-1)} - 2\mathrm{e}^{-\frac{y}{2}(\frac{r}{R_0}-1)}]. \tag{22}$$

MgO is an ionic crystal, so the Coulomb interaction should be considered. Each of the three pair potentials $\Phi_{\text{Mg–Mg}}(r)$, $\Phi_{\text{O–O}}(r)$ and $\Phi_{\text{Mg–O}}(r)$ comprises two parts: short-range and long-range interaction parts, the latter being the Coulomb interaction part:

$$\Phi_{\text{Mg–Mg}}(r) = \Phi^{\text{SR}}_{\text{Mg–Mg}}(r) + \Phi^{\text{Coul}}_{\text{Mg–Mg}}(r), \tag{23a}$$

$$\Phi_{\text{O–O}}(r) = \Phi^{\text{SR}}_{\text{O–O}}(r) + \Phi^{\text{Coul}}_{\text{O–O}}(r), \tag{23b}$$

$$\Phi_{\text{Mg–O}}(r) = \Phi^{\text{SR}}_{\text{Mg–O}}(r) + \Phi^{\text{Coul}}_{\text{Mg–O}}(r), \tag{23c}$$

where the superscripts 'SR' and 'Coul' mean the short-range part and the Coulomb interaction part, respectively. $\Phi^{\text{SR}}_{\text{Mg–Mg}}(r)$ and $\Phi^{\text{SR}}_{\text{O–O}}(r)$ are of the form of the Morse potential equation (22). $\Phi^{\text{Coul}}_{\text{Mg–Mg}}(r)$ and $\Phi^{\text{Coul}}_{\text{O–O}}(r)$ are of the same form:

$$\Phi^{\text{Coul}}_{\text{Mg–Mg}}(r) = \Phi^{\text{Coul}}_{\text{O–O}}(r) = \frac{Q^2_{\text{eff}}}{4\pi\varepsilon_0 r}. \tag{24}$$

The form of $\Phi^{\text{SR}}_{\text{Mg–O}}(r)$ is

$$\Phi^{\text{SR}}_{\text{Mg–O}}(r) = D_0\mathrm{e}^{y(1-\frac{r}{R_0})}, \tag{25}$$

which is called the 'exp-repulsive' potential. The expression for $\Phi^{\text{Coul}}_{\text{Mg–O}}(r)$ is

$$\Phi^{\text{Coul}}_{\text{Mg–O}}(r) = -\frac{Q^2_{\text{eff}}}{4\pi\varepsilon_0 r}. \tag{26}$$

The parameters in equations ((22), (24)–(26)) in these pair potentials are listed in tables 2 and 3.

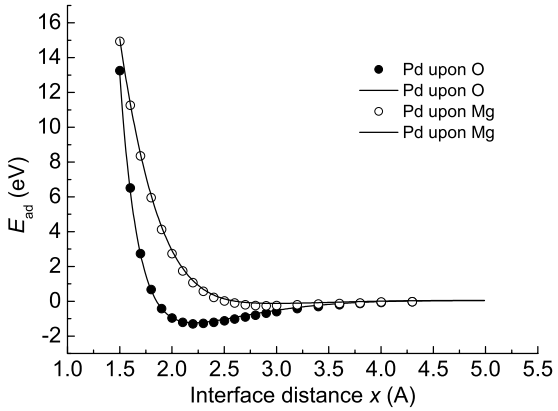

Figure 3. Adhesive energies of Pd/MgO(001) interface structures in figure 1 as functions of the interfacial distance x. Solid and open circles are *ab initio* results, and lines are from the summation of interatomic potentials using equations (1) and (2), respectively.

Table 3. Parameters in the pair potentials of bulk Pd.

Atom pair	Function form	D_0 (kcal mol^{-1})	R_0 (Å)	y
Pd–Pd	Morse	13.5372	2.9037	11.1404

2.3. Testing of the pair potentials

After the potentials have been obtained, a consistency check is necessary. To do this, the concept of adhesive energy should be introduced. If the total energy of a model is denoted as $E_{\text{total}}(x)$, the total energies of its two components, MgO and Pd, are denoted as E_{MgO} and E_{Pd}. The adhesive energy E_{ad} is defined as

$$E_{\text{ad}}(x) = E_{\text{total}}(x) - E_{\text{MgO}} - E_{\text{Pd}}. \tag{27}$$

Now there are two ways to calculate $E_{\text{ad}}(x)$ for the interface structure. One is to use *ab initio* computation, and the other is to sum all the possible potential energies using our inverted pair potentials. Figure 3 shows the comparison between the results obtained in the two ways. The good agreement shows that our inversion method is quite successful to this extent.

In fact, our inverted pair potentials can be applied to more interface structures besides those in figure 1. To show this, we further construct the following three virtual interface structures depicted in figure 4: Pd atoms are on top of the middle of Mg–O bond, the middle of O–O bond, and a quarter of the O–O bond. The E_{ad} curves generated by *ab initio* calculation and using the above pair potentials for these virtual structures are presented in figure 5. It is seen that the *ab initio* curves can be reproduced satisfactorily by our inverted pair potentials. This reveals that our potentials can reproduce the energy surface of Pd/MgO(001) to a great extent.

The models of figures 4(b) and (c) can represent the structure of the dislocation core to some extent. For example, in figure 4(b), Pd is on top of the middle of the O–O bond—it represents the structure in the middle of the dislocation core; and in figure 4(c), Pd is on top of a quarter of the O–O bond—it represents the structure near the middle of dislocation core. Figure 5 shows that the *ab initio* energy curves of figures 4(b) and (c) can be reproduced by the potentials to a great extent. This fitness supports the use of our pair potentials for misfit dislocations.

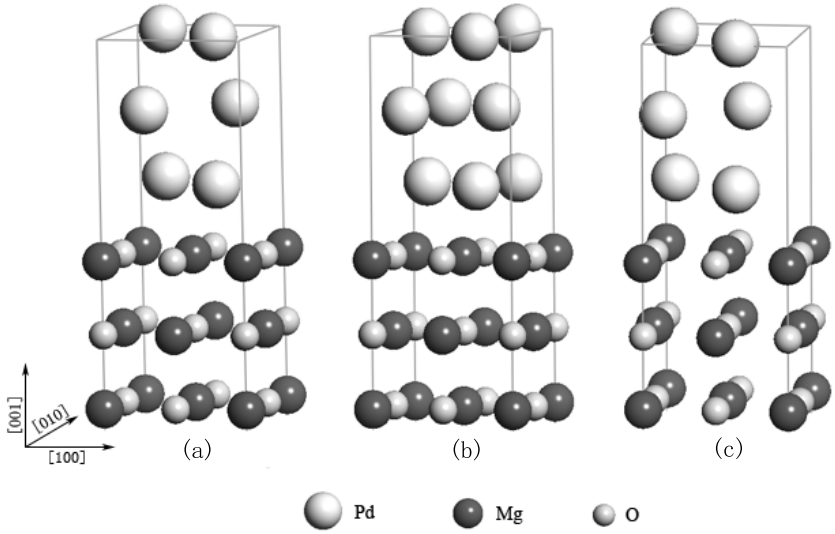

Figure 4. Virtual interface structures of Pd/MgO(001). (a) Pd on the middle of the Mg–O bond. (b) Pd on the middle of the O–O bond. (c) Pd on a quarter of the O–O bond.

According to our definition of adhesive energy, the lower the E_{ad}, the more stable the interface structure. It is easily seen from figure 3 that the structure of Pd upon Mg is not stable. Let us compare the other four structures in figure 1(a), figures 2(a)–(c). The lowest E_{ad} are -1.14, -0.65, -0.64, and -0.99 eV, respectively. Hence the structure of Pd upon O is the most stable one, which is just the structure observed in experiments [1, 2]. Therefore, all the investigations below take this model of the ideal interface as the starting structure.

Note that for the ideal interface, the lattice constant of Pd is equal to that of MgO. Nevertheless, our converted pair potentials are supposed to be applicable to any deformed or relaxed Pd/MgO(001) interface structure. In this way we can study this very complex mismatch dislocation system from a very easy starting point.

3. Study of the dislocation structure in 2D models

Pd has an fcc lattice, while MgO has a rock-salt lattice. Their experimental lattice constants are 3.889 and 4.216 Å respectively, with a relatively large misfit of -7.8%. This misfit causes the formation of dislocations on the Pd/MgO(001) interface.

Experiment shows that in Pd/MgO(001) the direction of the edge dislocation line (DL) is along $[1\bar{1}0]$ [3, 4], and the Burgers vector of the dislocation is $\frac{a}{2}[110]$, which is perpendicular to the DL. However, for bulk Pd the DL is along $[11\bar{2}]$, unlike that in the interface. This is because the slip plane in bulk Pd metal is (111), while in the Pd/MgO(001) interface, it has to be (001).

The existence of dislocations will influence the neighbouring atoms. The dislocation stress field is concentrated in the region near the DL. To catch the physics of dislocations, we first consider the DL in one direction. In an infinitely large system, the DL is infinite, and one merely needs to investigate the displacements of atoms in a plane perpendicular to the DL. This is a 2D model consisting of [001] and [110] directions, the former being perpendicular to and the latter being parallel to the interface. Figure 6 gives a perspective view of the model. The 2D model also helps to reduce computational time very much.

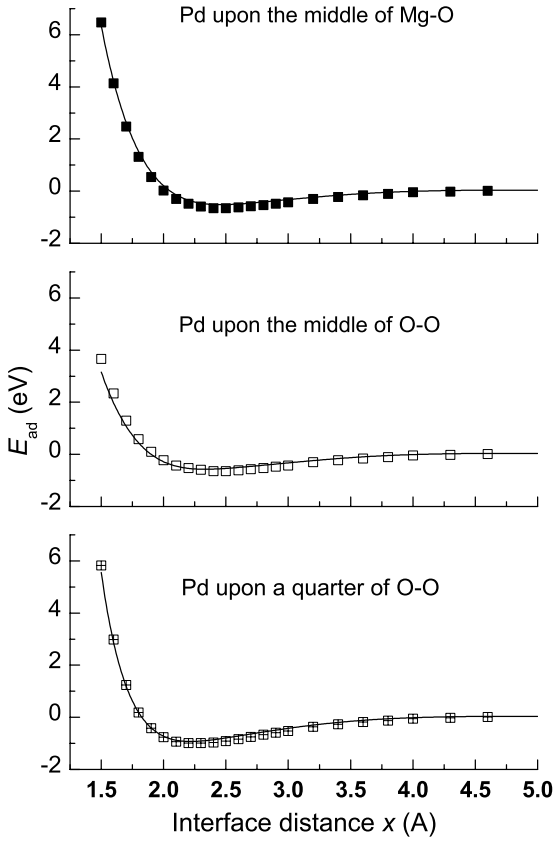

Figure 5. Adhesive energy curves from *ab initio* calculation and summation of potentials for the three virtual interface structures in figure 3. Squares represent the *ab initio* results and lines represent the summations of potentials.

Note that MgO is an ionic crystal, which is harder than a metal. This means that in the Pd/MgO(001) interface, the misfit dislocation appears on the metal side more easily. Therefore, in the following investigation the dislocations are constructed in the Pd side.

3.1. Structures of the dislocation core

To establish dislocation models, we first construct an ideal interface structure with a 6 ML MgO substrate and 16 ML of Pd. Hereafter the number of Pd layers is denoted as L_{Pd}. The model structure contains 281 Pd atoms and 102 MgO molecules so the total atom number is 485. The length of the cell along the [110] direction is 60.5 Å.

Here we explain why L_{Pd} is as high as 16 ML while the substrate has merely 6 ML. MgO is an ionic crystal. Its relaxation is much smaller than those of metals. Therefore, 6 ML MgO is enough for a substrate and a thicker substrate does not affect the interface. However, near the interface, Pd will relax, i.e., Pd atoms will deviate from their ideal positions. The displacement will be dependent on the distance to the interface and will be affected by the location of the DL.

On the basis of these considerations, we design initial dislocation models such that a slice of Pd atoms, along the (111) plane, is inserted into the ideal structure, with the edge being in

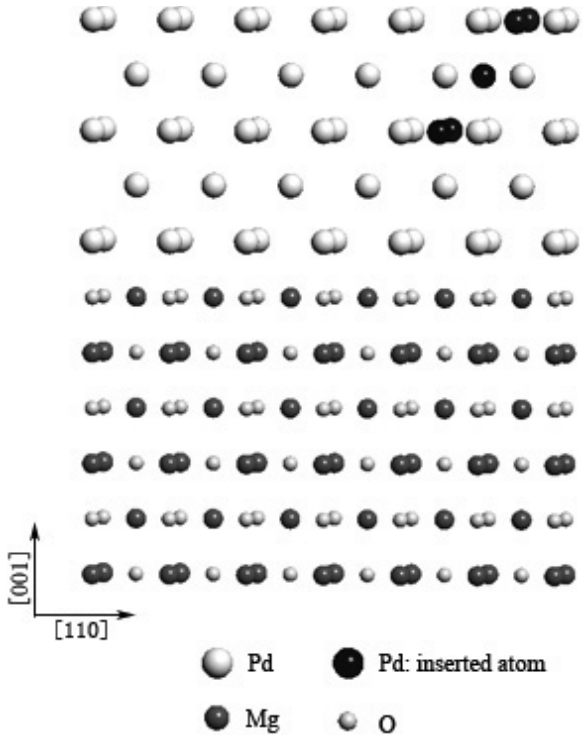

Figure 6. Perspective view of an example of the initial dislocation models: a slice of Pd atoms along the (111) plane is inserted into the ideal structure, with the edge (the DL) being in the third Pd ML from the interface.

the first to the eighth Pd ML from the interface. Figure 6 shows an example where the edge is in the third Pd ML from the interface. Hereafter, we write the identification number (ID) of the dislocation as n if the edge of the slice is in the nth ML from the interface. For instance, the ID of the model in figure 6 is 3.

Now we use atomistic relaxation to search for possible resulting dislocation structures using the MINIMIZER module of cerius2 [23] with our inverted pair potentials. The algorithm is SMART MINIMIZER.

After the atomistic relaxation, eight metastable atomic configurations of dislocations are obtained and they are shown in figure 7, with ID = 1–8. From the figure, we can see that each of them corresponds to a different location of the DL in the interface, from the first to the eighth ML. In other words, the ID denotes the position of the DL.

3.2. The stability of the dislocation structures

Since all the models in figure 7 are the results of relaxation, they should be at least metastable. To verify this we manipulate annealing by using the molecular dynamics method on the NPT ensemble, performed using the DYNAMICS SIMULATION module of cerius2 [23]. The time step is set at 0.001 ps. The temperature starts at 500 K, and goes through 400 K, 300 K, 200 K, 100 K, to 50 K, and then the model is relaxed. For each temperature, 10 000 steps were taken.

Figure 8 plots E_{total} before and after annealing. From the figure, the total energies of all the dislocation models have similar and small reductions after annealing. This means that

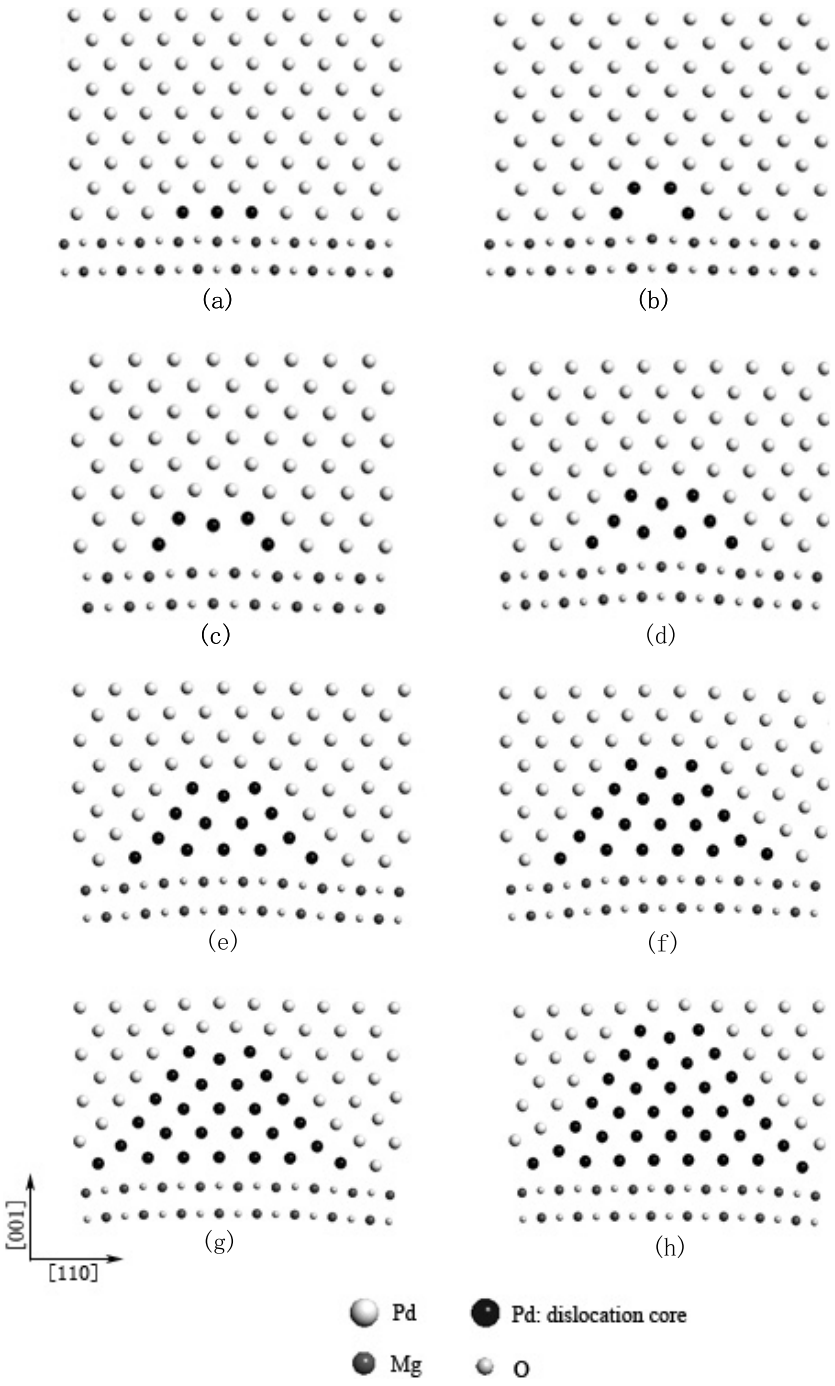

Figure 7. Some metastable dislocation core structures for Pd/MgO(001). ID = 1–8 for (a)–(h), respectively. Please note that in each model only 8 ML of Pd atoms and 2 ML of MgO are depicted.

these structures show no significant change, though there may be some positional relaxation of atoms.

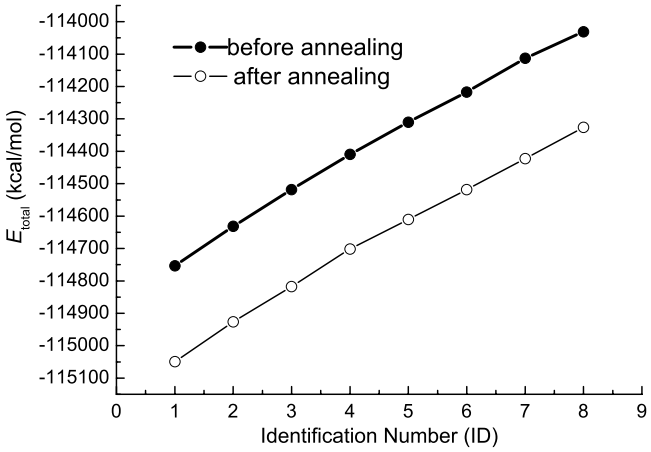

Figure 8. Total energies of the eight models in figure 7: solid and open circles represent the total energies before and after annealing, respectively. The lines are just to guide the eyes.

Table 4. Energy values in equation (28).

ε_{MgO} (kcal mol^{-1})	ε_{Pd} (kcal mol^{-1})	σ_{MgO} (kcal mol^{-1} Å^{-2})	σ_{Pd} (kcal mol^{-1} Å^{-2})	$\sigma_{interface}$ (kcal mol^{-1} Å^{-2})
−872.7314	−94.7055	2.4856	4.0927	4.1406

The model structure after annealing can also be depicted. The pictures reveal that all eight dislocation core structures in figure 7 remain unchanged upon annealing. Figure 9 shows an example with ID = 6. Figure 9(a) is just the model with ID = 6 from figure 7(f), and figure 9(b) is the resulting structure after annealing. It is seen that the dislocation structure remains unchanged and the Pd atom positional adjustment of atoms is trivial.

3.3. The most stable dislocation structure

It is seen in figure 7 that for ID = 1–4, the substrate surface becomes more and more convex. This reflects the stress becoming stronger as the ID goes from 1 to 4, while as the ID goes from 4 to 8, the stress becomes weaker, as shown in figure 7. Therefore, when ID = 4, the stress is the strongest.

However, the total energy contains various contributions coming from the dislocation, surface, interface and bulk. To describe the stress around the dislocation properly, we introduce the dislocation energy per unit interface area E_{dis} defined as

$$E_{dis} = \frac{E_{total} - n_{MgO}\varepsilon_{MgO} - n_{Pd}\varepsilon_{Pd}}{S} - (\sigma_{MgO} + \sigma_{Pd} + \sigma_{interface}). \tag{28}$$

In equation (28), S denotes the interface area, n_{MgO} and n_{Pd} denote the numbers of MgO molecules and Pd atoms, respectively, and ε_{MgO} and ε_{Pd} denote the energies per MgO molecule and per Pd atom in the respective bulk materials. The last three terms in equation (28) are surface energies per unit area: σ_{MgO} and σ_{Pd} are those of MgO and Pd surfaces and $\sigma_{interface}$ is that of the model of figure 1(a). The energy values appearing in equation (28) are listed in table 4.

The models in figure 7 have fixed L_{Pd}, all with 16 ML. In order to consider the effect of the Pd layer thickness on the dislocation structure, we also construct models with different

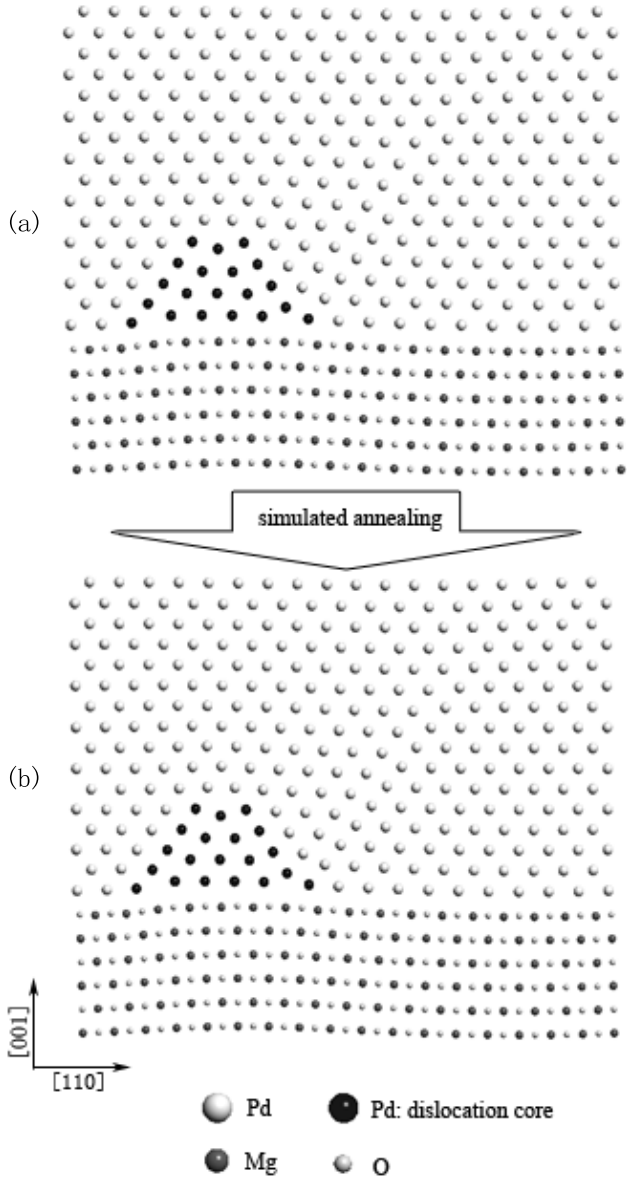

Figure 9. Dislocation structures of figure 7(f) with ID = 6 (a) before and (b) after simulated annealing.

L_{Pd}. In these models, the L_{Pd} goes from 3 to 10 ML. If the $L_{Pd} = m$ ML, we construct dislocation models similar to that in figure 6 with the ID being 1 to $m - 1$. For example, when $L_{Pd} = 3$ ML, the ID can be 1 or 2. Let us compare the dislocation energies of these cases.

Figure 10 plots E_{dis} of the models with different L_{Pd} and ID for each fixed L_{Pd}. It is easily seen that the model with ID = 1 has the lowest E_{dis} for each fixed L_{Pd}. So, the dislocation structure with ID = 1 is regarded as the most stable. When ID = 4, the model has the highest E_{dis}; thus it is the most unstable metastable dislocation structure. This is in agreement with the picture in figure 7 where the substrate is most strongly convex for ID = 4.

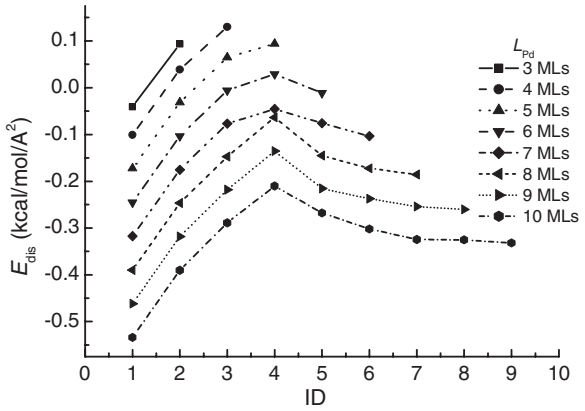

Figure 10. Dislocation energy $E_{\rm dis}$ as a function of $L_{\rm Pd}$ and ID. The lines are just to guide the eyes.

Figure 10 shows that when ID < 4, the dislocation energy $E_{\rm dis}$ increases with ID; and when ID > 4, $E_{\rm dis}$ decreases with ID. If the ID is large enough, say larger than 7, $E_{\rm dis}$ becomes nearly invariant. This feature can be presented in an intuitive way. If we assume that a metastable edge dislocation appears in the first to fourth ML from the interface, or with the ID < 4, it will probably be attracted to the interface so as to lower the $E_{\rm dis}$. And if a metastable edge dislocation is assumed to appear with an ID more than 4, it will probably climb away from the interface to lower the $E_{\rm dis}$.

3.4. The investigation of the dislocation density

As has been mentioned in the last subsection, the most stable dislocation structure near the interface is that with ID $= 1$. Therefore, hereafter we investigate the structures with ID $= 1$. In this subsection we seek possible dislocation densities at the interface for fixed $L_{\rm Pd}$.

For each $L_{\rm Pd}$, we insert a slice of Pd atoms just as in figure 6 but with ID $= 1$. Then along the direction perpendicular to the DL, we choose a different cell length to artificially produce the dislocation density. The range of cell length is from 33 to 122 Å, and the corresponding dislocation density goes from 0.008 to 0.027 Å^{-1}. The structures are relaxed by means of the method used in section 3.1. After relaxing, $E_{\rm dis}$ is calculated using equation (28).

Figure 11 plots $E_{\rm dis}$ with the variation of dislocation density for $L_{\rm Pd}$ being from 2 to 16 ML. Let us first look at the case $L_{\rm Pd} = 2$ ML. In this case, $E_{\rm dis}$ decreases almost linearly as the dislocation density decreases. Therefore, we consider that the density should be small enough to be negligible.

It is worthy of note that from the atomistic relaxation, when there is just one Pd ML, there is no dislocation formed. The inserted atom will be piled out from the Pd ML. Figure 12 depicts the structures before and after relaxing for $L_{\rm Pd} = 1$ and 2.

When $L_{\rm Pd} \geqslant 3$, there appears a minimal energy in each curve in figure 11. The energy minimum moves to the right as $L_{\rm Pd}$ increases. When $L_{\rm Pd} \geqslant 11$, the position of minimal energy is unchanged with varying $L_{\rm Pd}$ and keeps at the dislocation density 0.019 Å^{-1}. Figure 13 shows the minimal dislocation density as a function of $L_{\rm Pd} \geqslant 3$.

In summary, the dislocation density in the Pd/MgO(001) interface increases slightly with the Pd layer thickness, and when $L_{\rm Pd} \geqslant 11$, it is about 0.019 Å^{-1}.

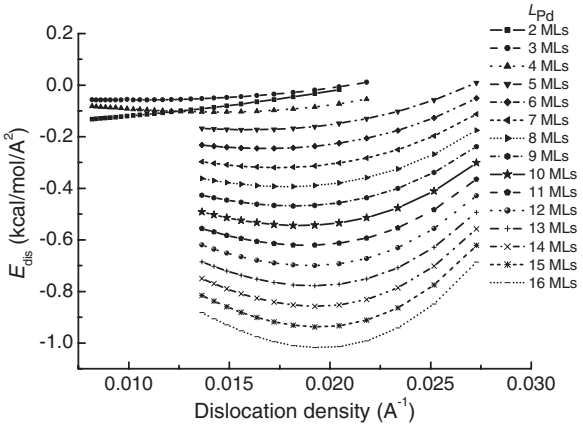

Figure 11. Dislocation energy E_{dis} as a function of dislocation densities for $L_{\mathrm{Pd}} = 2$ to 16 ML. ID = 1.

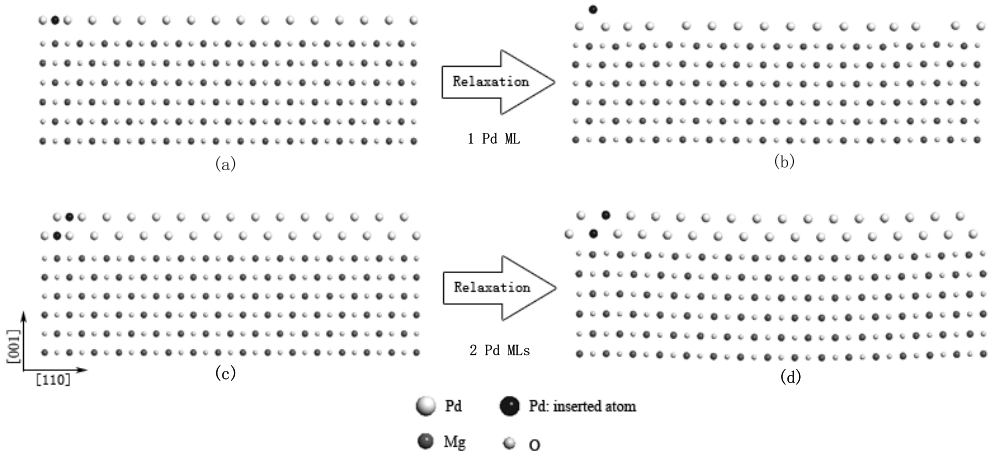

Figure 12. Structures before and after relaxing when ID = 1 and $L_{\mathrm{Pd}} = 1, 2$ ML. When $L_{\mathrm{Pd}} = 1$, the structures are (a) before relaxing and (b) after relaxing. It is obvious that the inserted atom is piled out. When $L_{\mathrm{Pd}} = 2$, the structures are (c) before relaxing and (d) after relaxing.

3.5. The bond distribution around the dislocation

Because of the misfit of the interface, Pd atoms may deviate from their ideal positions and the bond length between nearest neighbour atoms near the interface may not be unique. In figure 14, we plot the Pd–Pd bond length distribution of the first-ML Pd atoms upon MgO along the [110] direction for an $L_{\mathrm{Pd}} = 5$ model. We also plot in figure 14 the Pd–O bond lengths across the interface along the same direction. The two bond lengths vary with the same period. When Pd is just on top of an O atom, the Pd–O bond length is the smallest. Then the neighbouring Pd–Pd bond length will be the greatest. If a Pd atom deviates from the position upon the O atom, which corresponds to the dislocation core, the Pd–O bond length will be greater. And then the neighbouring Pd atoms will be closer and their bond lengths will be smaller. Figure 14 clearly shows that the greatest Pd–O bond length corresponds to the smallest Pd–Pd bond length and the smallest Pd–O bond length corresponds to the greatest

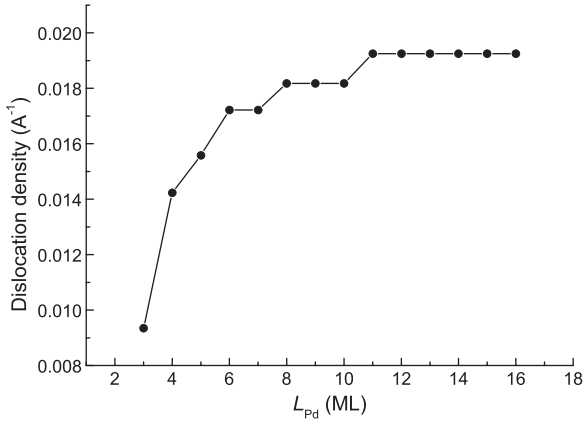

Figure 13. Dislocation density at which the dislocation energy is minimal as a function of $L_{\mathrm{Pd}} \geqslant 3$. The line is just to guide the eyes.

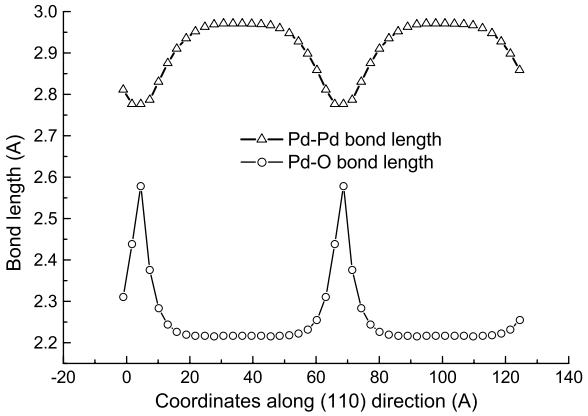

Figure 14. Distribution of Pd–Pd and P–O bond lengths along the [110] direction for $L_{\mathrm{Pd}} = 5$. The Pd and O atoms are at the first monolayer from the interface. The lines are just to guide the eyes.

Pd–Pd bond length. The periodicity of the bond length distribution shown in figure 14 also reflects a regular distribution of dislocation lines on the interface. Therefore, the interface is semi-coherent.

Figure 15 depicts the interface structure of the model. The black balls underline the positions of dislocation cores. The positions of the dislocation cores correspond to the peaks of the Pd–O bond length curve in figure 14. It is obvious that the DL distributes periodically and the picture of a semi-coherent interface is quite clear.

3.6. The condition for generation of a dislocation from an ideal interface

In the above subsections, we inserted an extra Pd slice into the ideal interface so as to construct dislocation structures. Now we investigate the case if we do not insert the extra slice: what will the interfacial structure become after relaxing?

Ideal interface models are constructed with the Pd film thicknesses of 1–16 ML. The cell length along the interface direction is chosen as 61 Å. Figures 16(a) and (c) plot as examples the

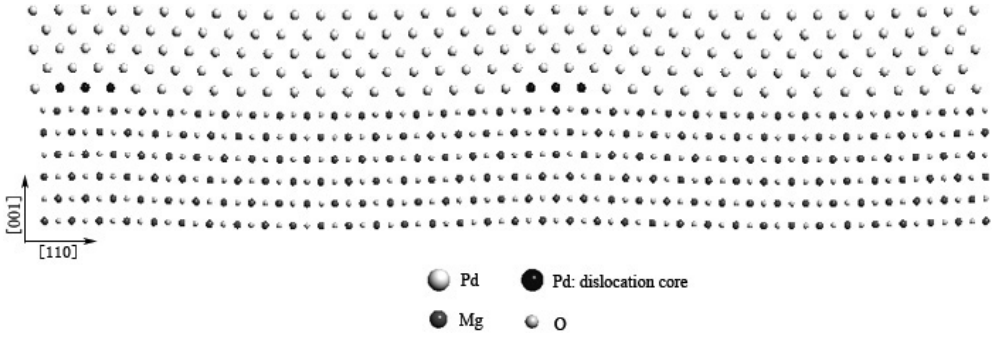

Figure 15. The semi-coherent Pd/MgO(001) interface for $L_{\mathrm{Pd}} = 5$.

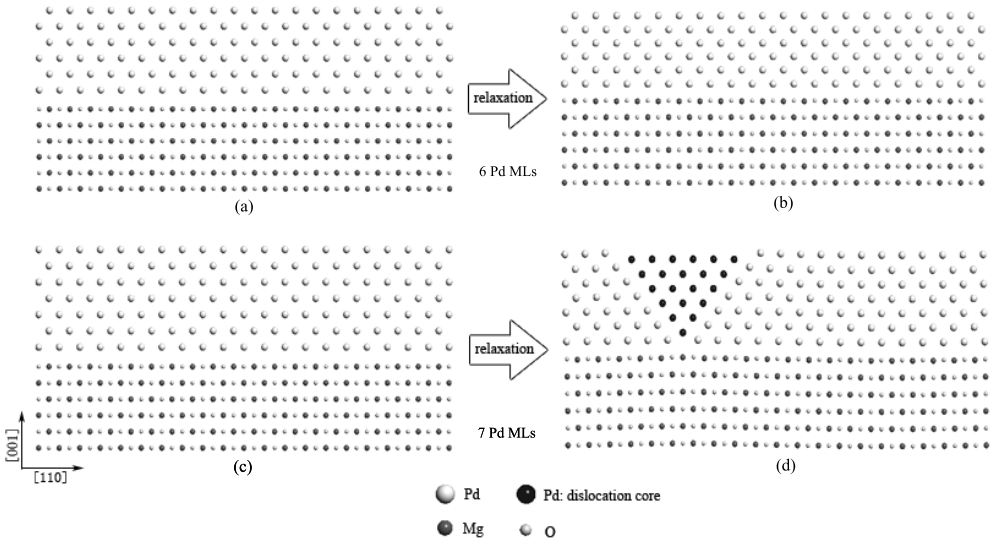

Figure 16. Relaxation of ideal interfaces. (a) and (c) are ideal interface structures before relaxing with $L_{\mathrm{Pd}} = 6$ and 7 ML, respectively. (b) and (d) are the corresponding structures after relaxing. It is seen that in (b) the ideal interface is not destroyed, while in (d) the ideal interface is destroyed and the substrate is convex where the DL is formed.

two models with $L_{\mathrm{Pd}} = 6$ and 7 ML, respectively. In order to find the most stable structures, every atom in the Pd layer is displaced randomly by 0.5 Å. Then the model structures are relaxed until the minimum total energies are reached.

The results show that if $L_{\mathrm{Pd}} \leqslant 6$ ML, the ideal interface is not destroyed and there is no DL generated; see figure 16(b) for an example. However, when $L_{\mathrm{Pd}} \geqslant 7$ ML, the ideal interface is destroyed and the DL appears with ID = 1, as shown in figure 16(d).

In this subsection the cell length is 61 Å, so if there is a dislocation, the dislocation density of this model is 0.0164 $\mathrm{Å}^{-1}$. Therefore, the definition of an 'ideal interface' here can also be regarded as 'one with dislocation density less than 0.0164 $\mathrm{Å}^{-1}$'. From figure 13, we see that the dislocation density is larger than 0.0164 $\mathrm{Å}^{-1}$ when $L_{\mathrm{Pd}} > 5$ ML. It is one ML smaller than the result of this subsection. This difference is ascribed to the different computational model.

We have mentioned above that dislocations should appear in the Pd layer and that the case of ID = 1 is the most stable. In this subsection, we do not insert an extra slice. We see that the dislocation naturally appears, with its structure similar to that of the ID = 1 model.

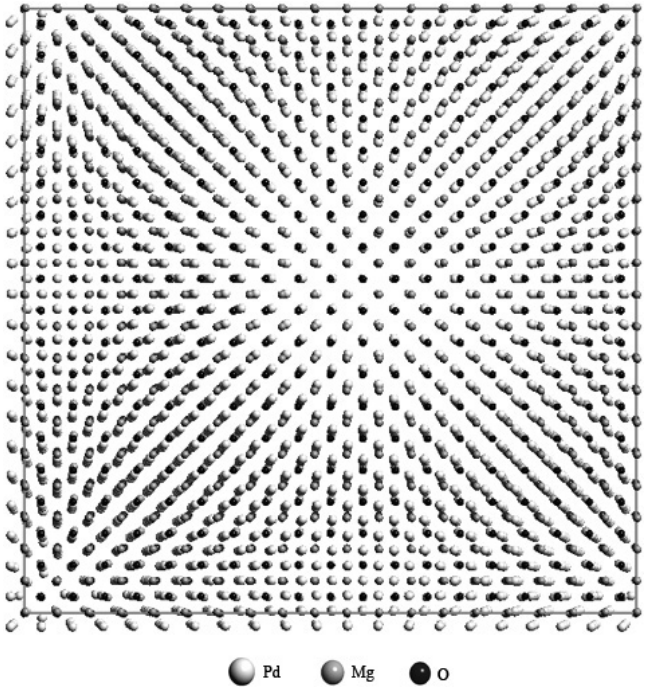

Figure 17. 3D interface model which contains perpendicularly intersecting dislocations. The view is in the [001] direction. This is a 58 Å × 58 Å cell, containing 6726 atoms.

4. Study of the dislocation structure in 3D models

In section 3, we investigated 2D models; as in figure 6, there are only two ML considered along the DL. Although the models were simplified, they did provide clear and straightforward pictures of the possible exhibiting of dislocations. Furthermore, the conclusions achieved in section 3 are helpful to us in investigating 3D models.

Now, we will study 3D models; i.e., there are finite lengths along the directions $[1\bar{1}0]$ and [110] of the interface model. This inevitably causes the computation time to increase greatly. Figure 17 shows a 3D interface model which contains perpendicularly intersecting dislocations. The model is 58 Å in length and width, with 6726 atoms.

In this section, L_{Pd} goes from 3 to 15 ML, and the ID of the dislocations in all models is set to 1. For each L_{Pd}, ideal structure is established, and then extra slices of Pd atoms are inserted along both (111) and $(1\bar{1}1)$ planes. The dislocation density along each of the directions is determined from figure 13, which corresponds to the cell length of the interface model. After relaxing, the adhesive energy E_{ad} is calculated using equation (17), and the interface distance x_0 is obtained from the equilibrium model. Figure 17 plots x_0 and the corresponding E_{ad} as functions of L_{Pd}.

The physical properties obtained in the 2D case are still valid in the 3D case. For instance, the dislocation picture along the [110] direction is the same as the one along the $[1\bar{1}0]$ direction. If we count the bond lengths and depict the structure along the [110] direction, we will get the same curves as in figure 14 and a picture as in figure 15.

In figure 18, E_{ad} decreases with increase of L_{Pd}, which is consistent with the *ab initio* computational data from Giordano [12] and Goniakowski [10].

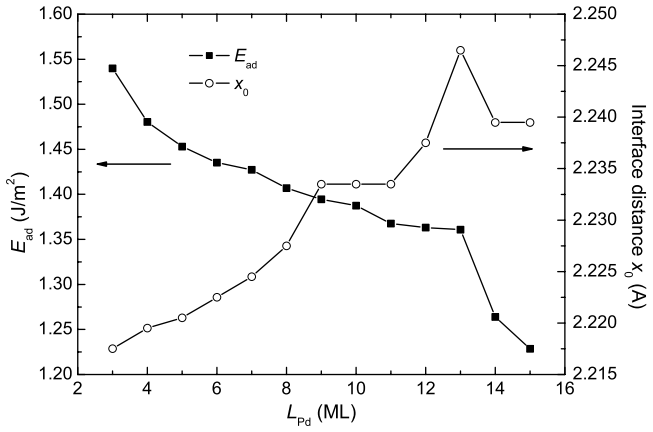

Figure 18. Adhesive energy E_{ad} and interface distance x_0 as functions of L_{Pd} in 3D models. DLs are along both [1$\bar{1}$0] and [110] directions, and dislocation densities are determined from figure 13. The lines are just to guide the eyes.

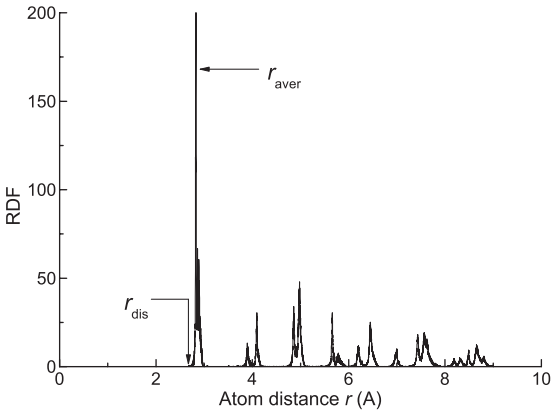

Figure 19. RDF of the relaxed 3D model with $L_{Pd} = 10$ ML.

It is found that x_0 is dependent on L_{Pd}. Figure 18 shows that x_0 rises with increase of L_{Pd}, which is consistent with the decreasing of E_{ad}. As the interface distance rises, the Pd–O bond length increases, so E_{ad} decreases.

In figure 18, the interfacial distance is between 2.218 and 2.247 Å. Experiments showed that the interfacial distance increased with the Pd film thickness [6] and its value was 2.22 ± 0.03 Å [1, 2]. Our theoretical results agree with the experimental results quite well.

From figure 14, we acquire the idea that the Pd–Pd bond will be compressed at the dislocation core. In 3D cases, the conclusion is the same. Figure 19 plots the Pd–Pd radial distribution function (RDF) of the relaxed model with $L_{Pd} = 10$ ML. Each peak has a width. In contrast, if the interface is ideal, every peak will have zero width. Let us look at the first peak in figure 19. The peak position is marked as r_{aver}, which is the averaged Pd–Pd bond length. The shortest Pd–Pd bond length is denoted as r_{dis}, which is the front edge of the first peak. It is the bond length at the dislocation core.

In figure 20, we plot r_{aver} and r_{dis} as a function of L_{Pd}. It is seen that when $L_{Pd} < 6$ ML, the average bond length r_{aver} is some 2.86 Å, greater than the bulk length 2.83 Å, which means

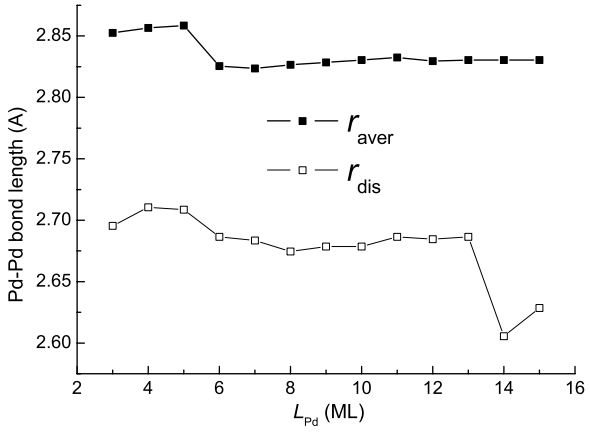

Figure 20. r_{aver} and r_{dis} as functions of L_{Pd} in 3D models: DLs are along both $[1\bar{1}0]$ and [110] directions, and dislocation densities are determined by figure 13. The lines are just to guide the eyes.

that the Pd film is expanded by the MgO substrate. When $L_{Pd} \geqslant 6$, r_{aver} is some 2.83 Å, close to the bulk value. This is the contribution of misfit dislocations. Correspondingly, r_{dis} in the cases with $L_{Pd} \geqslant 6$ is larger than that in the cases with $L_{Pd} < 6$ ML. Comparing figure 20 with 14, one sees that the shortest Pd–Pd bond length in the 3D case is less than that in the 2D case, which is caused by the intersecting DLs. Pd–Pd is much more compressed at the point of intersection.

5. Conclusions and discussion

By constructing ideal and virtual Pd/MgO(001) interface structures and applying the Chen–Mobius inversion method, we obtain interatomic pair potentials Φ_{Pd-Mg} and Φ_{Pd-O} across the Pd/MgO(001) interface from *ab initio* adhesive energies. Testing them with other interface structures shows that the potentials apply to the interface well.

By means of the pair potentials across the interface obtained in this paper and those for bulk materials obtained before, possible dislocation structures near Pd/MgO(001) interfaces are investigated systematically. Atomistic relaxation and molecular dynamics studies are performed to achieve stable interface structures.

The investigations of 2D models provide some clear physical pictures of the dislocations. If an extra slice of Pd atoms is inserted, dislocations are formed. Figure 7 shows some metastable misfit dislocation structures of Pd/MgO(001). From the analysis of figure 10, we see that the DL in the first Pd ML is the most stable structure.

When $L_{Pd} = 1$ and 2, there is no dislocation generated, although the Pd atoms at the interface undergo relaxation, as shown in figure 12. When L_{Pd} increases, DLs appear and the dislocation density increases slightly with L_{Pd}. When $L_{Pd} \geqslant 11$, the dislocation density remains about 0.019 A^{-1}.

The atomic arrangement near the interface is shown in figure 14, and figure 15 gives an intuitive picture of the semi-coherent interface. Both the Pd–Pd bond length in the first ML from the interface and the Pd–O bond length across the interface are distributed periodically, reflecting the interface being semi-coherent.

If there is no extra slice of Pd atoms inserted, the DL will not appear for $L_{Pd} \leqslant 6$. In this case the interface is ideal, i.e. the Pd atoms near the interface do not relax and every Pd atom in the first ML is just upon an O atom. When $L_{Pd} \geqslant 7$, the DL will appear.

We have reasoned that dislocations should appear in the Pd layer, so an extra slice of Pd atoms is inserted to produce dislocations in sections 3.1–3.5. The results indicate that the dislocation structures with ID = 1 are the most stable. In section 3.6, we do not insert an extra slice. We see that after relaxation the dislocations naturally appear in the Pd layer with a structure similar to that of the ID = 1 model.

The physical pictures established in the 2D model are still valid for 3D models. In 3D models, DLs intersect perpendicularly in the interface. The resulting interfacial distance x_0 increases with L_{Pd}. The values of x_0, as well as its tendency, are in good agreement with experiments. The adhesive energy E_{ad} decreases with increase of L_{Pd}, which is consistent with the *ab initio* computational data obtained by others.

Since the inversion method described in section 2 is a key step in providing necessary pair potentials for studying the interface, we here give more discussion by pointing out several remarkable features of the method.

(1) There is a neat formula for extracting pair potentials from adhesive energies, as shown by equation (19).
(2) Unlike the conventional empirical potentials fitted from experimental data, the present pair potentials are directly extracted from *ab initio* adhesive energy curves and no special function forms of the potential are assumed beforehand.
(3) These pair potentials are obtained from interface models without misfit, and we use them to investigate the equilibrium structures and misfit dislocations.
(4) The *ab initio* energies have been calculated for a wide range of interface distances, so that more information can be reproduced using the converted pair potentials, not just the adhesive energy of the equilibrium structure. In addition, both the low energy state (figure 1(a)) and the high energy state (figure 1(b)) structures have been used for inversion. Therefore, except for the equilibrium structures, our pair potentials are also applicable for non-equilibrium states or excited states of the interface systems.

Finally, we ought to point out an important discrepancy between the inversion of pair potentials across the interface and in the bulk: in the former case the Mobius transformation makes use of the additive semigroup as shown in equation (15), while in the latter case the transformation makes use of the multiplicative semigroup as shown by equation (20). In mathematics, the additive Mobius transformation equation (15) is an extension of the original multiplicative Mobius transformation equation (20). In physics, this reflects the fact that the interface systems should be described using the additive semigroup, while the bulk systems should be described using the multiplicative semigroup.

Acknowledgments

This work was supported by the National Advanced Materials Committee of China. Also, the authors gratefully acknowledge the financial support from the 973 Project in China under Grant No G2000067101.

References

[1] Renaud G and Barbier A 1999 *Surf. Sci.* **433–435** 142
[2] Renaud G, Barbier A and Robach O 1999 *Phys. Rev.* B **60** 5872
[3] Lu P and Cosandey F 1992 *Acta Metall. Mater.* **40** S259
[4] Chen F R *et al* 1994 *Ultramicroscopy* **54** 179
[5] Fornander H *et al* 1998 *J. Cryst. Growth* **186** 189

[6] Fornander H *et al* 1996 *Appl. Phys. Lett.* **68** 2636
[7] Graoui H, Giorgio S and Henry C R 1998 *Surf. Sci.* **417** 350
Graoui H, Giorgio S and Henry C R 2001 *Phil. Mag.* B **81** 1649
[8] Henry C R and Meunier M 1996 *Mater. Sci. Eng.* A **217/218** 239
[9] Haas G *et al* 2000 *Phys. Rev.* B **61** 11105
[10] Goniakowski J 1998 *Phys. Rev.* B **57** 1935
Goniakowski J 1998 *Phys. Rev.* B **58** 1189
Goniakowski J 1999 *Phys. Rev.* B **59** 11047
[11] Goniakowski J and Noguera C 1999 *Phys. Rev.* B **60** 16120
[12] Giordano L, Goniakowski J and Pacchioni G 2001 *Phys. Rev.* B **64** 075417
[13] Wu R Q and Freeman A J 1995 *Phys. Rev.* B **51** 8
[14] Yamauchi R *et al* 1998 *Appl. Surf. Sci.* **130–132** 572
[15] Endou A *et al* 2000 *J. Appl. Phys.* **39** 4255
[16] Vervisch W, Motter C and Goniakowski J 2002 *Phys. Rev.* B **65** 245411
[17] Chen N X 1990 *Phys. Rev. Lett.* **64** 1193
[18] Chen N X and Rong E Q 1998 *Phys. Rev.* E **57** 1302
[19] Zhang S and Chen N X 2003 *Modelling Simul. Mater. Sci. Eng.* **11** 331
Zhang S and Chen N X 2003 *Mater. Sci. Eng.* B **99** 588
Zhang S and Chen N X 2003 *Phil. Mag.* **83** 1451
[20] Hao S Q, Chen N X and Shen J 2002 *Phys. Status Solidi* b **234** 487
[21] Zhang S and Chen N X 2005 *Chem. Phys.* **309** 309
[22] Long Y, Chen N X and Zhang W Q 2005 *J. Phys.: Condens. Matter* **17** 2045
[23] Accelrys Inc. *CASTEP Users Guide*
[24] Milman V *et al* 2000 *Int. J. Quantum Chem.* **77** 895
[25] Monkhorst H J and Pack J D 1976 *Phys. Rev.* B **13** 5188
[26] Macdonald A H 1978 *Phys. Rev.* B **18** 5897
[27] Chen N X and Shen J 1992 unpublished
[28] Zhang S 2002 *PhD Thesis* Tsinghua University